Title

Practical aspects of prostate MRI: hardware and software considerations, protocols, and patient preparation.

Journal

Abdominal radiology (New York), 41(5)

ISSN

2366-004X

Authors

Starobinets, Olga
Korn, Natalie
Iqbal, Sonam
et al.

Publication Date

2016-05-01

DOI

10.1007/s00261-015-0590-x

Peer reviewed

Abdominal Radiology

Published online: 21 December 2015

Abdom Radiol (2016) 41:817–830
DOI: 10.1007/s00261-015-0590-x

Practical aspects of prostate MRI: hardware and software considerations, protocols, and patient preparation

Olga Starobinets,[1] Natalie Korn,[1] Sonam Iqbal,[1] Susan M. Noworolski,[1] Ronald Zagoria,[2] John Kurhanewicz,[3] Antonio C. Westphalen[2]

[1]Graduate Group of Bioengineering, Department of Radiology and Biomedical Imaging, University of California San Francisco, 185 Berry Street, Box 0946, San Francisco, CA 94143, USA

[2]Department of Radiology and Biomedical Imaging, University of California San Francisco, 505 Parnassus Avenue, M372, Box 0628, San Francisco, CA 94143, USA

[3]Graduate Group of Bioengineering, Department of Radiology and Biomedical Imaging, University of California San Francisco, 1700 4th Street, Ste. 203, San Francisco, CA 94158, USA

Abstract

The use of multiparametric MRI scans for the evaluation of men with prostate cancer has increased dramatically and is likely to continue expanding as new developments come to practice. However, it has not yet gained the same level of acceptance of other imaging tests. Partly, this is because of the use of suboptimal protocols, lack of standardization, and inadequate patient preparation. In this manuscript, we describe several practical aspects of prostate MRI that may facilitate the implementation of new prostate imaging programs or the expansion of existing ones.

Key words: Prostate—Magnetic resonance—Technique—Protocol

Multiparametric magnetic resonance imaging (mpMRI) of the prostate combines anatomic with functional and physiological assessment of the gland, and encompasses various sequences, including T1- and T2-weighted MR imaging, diffusion-weighted imaging (DWI) and apparent diffusion coefficient (ADC) maps, dynamic contrast-enhanced (DCE) MRI, and sometimes proton magnetic resonance spectroscopic imaging (1H-MRSI) [1–3], as shown in Fig. 1. As such, in addition to the anatomic data, the mpMRI exam offers information about the microscopic mobility of water (Brownian motion), biochemical characteristics, neovascularity, and cellular structure of the prostatic tissue. Since these characteristics are different for malignant and benign tissues, high-resolution mpMRI provides valuable data that helps characterize the extent and biological behavior of prostate cancer. Owing to these capabilities, MR imaging of the prostate is increasingly being used to assist patients and clinicians to make management decisions [4–8].

The mpMRI exam offers a comprehensive assessment of prostatic tissues using an array of metrics that can be tailored according to the patient's clinical need. Among the main patient-specific factors that determine optimal mpMRI, performance is the patient treatment history [9]. The imaging metrics most relevant to diagnosis may change for imaging patients after radiation [10, 11], focal brachytherapy [12], hormone treatment [13, 14], and/or surgery [13, 15, 16]. Additionally, implants associated with abdominal and pelvic comorbidities—such as hip replacements [17, 18] or lumbar fusions [19]—can significantly affect image quality for certain modalities. This detrimental effect of implants on MR imaging is changing with increased usage of non-metallic implants [20]. Irrespective of the imaging center's abilities to perform an mpMRI, the individual patient history will dictate the most appropriate imaging metrics to include for diagnosis.

Multiparametric MRI of the prostate, however, is still plagued by lack of standardization, which in turn leads to a heterogeneous performance of the method. In part aiming at this problem, the American College of Radiology (ACR), the European Society of Urogenital Radiology, and the AdMeTech Foundation have pro-

Correspondence to: Antonio C. Westphalen; *email:* antonio.westphalen@ucsf.edu

posed the use of the Prostate Imaging Reporting and Data System (PI-RADS), now in its second version [3]. In that document, the ACR describes, among other important aspects of mpMRI, the minimum recommended parameters for imaging patients. In this article, we discuss various aspects of imaging acquisition and suggest two protocols that may be used for adequate assessment of patients with prostate cancer.

Hardware and software considerations

Multiparametric prostate imaging was initially implemented on 1.5-Tesla (1.5T) scanners [21–29]. To acquire scans with diagnostic value, both a pelvic phased array and an endorectal coil (ERC) were used in combination [30]. In prostate MR imaging, ERCs provide a significant improvement in signal-to-noise ratio (SNR) and spatial resolution when compared to pelvic phased array coils alone [31]. This has a profound impact on the quality of the SNR-starved functional imaging, i.e., 1H-MRSI and DWI. Traditional ERCs use a balloon-filled coil that achieves nine-fold SNR improvement over a phased array alone [31]. After insertion into the rectum, the balloon is inflated, with 40–80 ml of either an inert fluid that matches the susceptibility of the prostatic tissues, e.g., perfluorocarbon (PFC) or barium sulfate [31], or alternatively with air or water. Using an inert fluid instead of air or water improves the homogeneity of the magnetic field and decreases susceptibility artifacts between the rectum and the prostate [32, 33]. These inflatable ERCs provide better coverage, are associated with fewer motion artifacts, and are faster to position when compared to rigid coils [31]. Using either a rigid or an inflatable ERC will create an inhomogeneous reception profile which results in higher signal intensity (SI) near the rectal wall and may hinder cancer detection in the peripheral zone. Fortunately, this signal non-uniformity can be easily rectified using readily available coil-correction software [34].

The introduction of 3-Tesla (3T) clinical scanners presents an opportunity to enhance image quality by trading the increased SNR for improvements in spatial and temporal resolutions, decreasing the necessity of an ERC. However, the SNR increase provided by an ERC can only be partially replaced by a two-fold SNR improvement associated with doubling the magnet strength. Nevertheless, with advances in pulse sequence design, several groups reported that studies done solely with 6 to 32 phased array surface coils at 3T yielded comparable images as the exams conducted with 1.5T scanners with an endorectal coil [35–39]. Comparison studies with and without ERC at 3T have shown increased sensitivity (0.45, no ERC and 0.75, with ERC) and positive predictive value (0.64, no ERC and 0.80, ERC) for prostate cancer detection [40] (Fig. 2). However, considering patient discomfort, patient preparation, costs, coil placement time, and anatomical distortion associated with ERCs, the use of ERCs in prostate imaging is still being actively debated.

Various commercially available and proprietary softwares are used for advanced assessment of MR images. These include software for post-processing of DWI, MRSI, and, most commonly, DCE data. While these technologies are not essential for imaging interpretation, they often improve the workflow in the reading room by optimally displaying the various MR data, which in turn leads to faster analyses, interpretation [41], and reporting [42]. These systems have also been shown to increase the confidence of less experienced readers [43]. Furthermore, many of these softwares are now used to prepare the MR data for fusion with ultrasound images in MR targeted biopsy systems [44].

Protocols

Patients are usually scanned in the supine position to maximize patient comfort and minimize respiratory-induced prostate motion between acquisitions. However, when an ERC is not used, the prone position may be a better alternative for some men. Imaging patients in the prone position can result in higher respiratory motion artifacts but may be necessary to facilitate comfort for certain patients [45, 46]. MR imaging of the prostate begins with a low-resolution 3-plane localizer ‘scout.’ These images are used to locate the prostate and establish the orientation of the coils in relation to the gland prior to scanning. If an endorectal coil is used, then particular attention should be paid to the sagittal scout and axial images, and any adjustments in ERC placement and rotation must be made before time-intensive scanning begins. Guidelines for 3T MRI acquisition parameters based on the protocol used at our institution are summarized in Table 1 (with an ERC) and Table 2 (without an ERC).

T1-weighted MR imaging

A multiparametric MR imaging exam of the prostate typically includes an axial large field-of-view T1-weighted scan of the entire pelvis to assess regional lymph nodes for abnormal size, shape, or intensity. Identification of these lymph nodes is facilitated by the T1 contrast between the high signal intensity of visceral fat and lower signal intensity of large or irregularly shaped lymph nodes [47]. To ensure that lymph nodes in the drainage pathway are imaged during the exam, the T1-weighted scan prescription should extend superiorly to the aortic bifurcation [48]. T1-weighted imaging is also useful to diagnose post-biopsy hemorrhage, which demonstrates high signal intensity [47]. Hemorrhage often has low T2 signal intensity, mimicking cancer, and may introduce

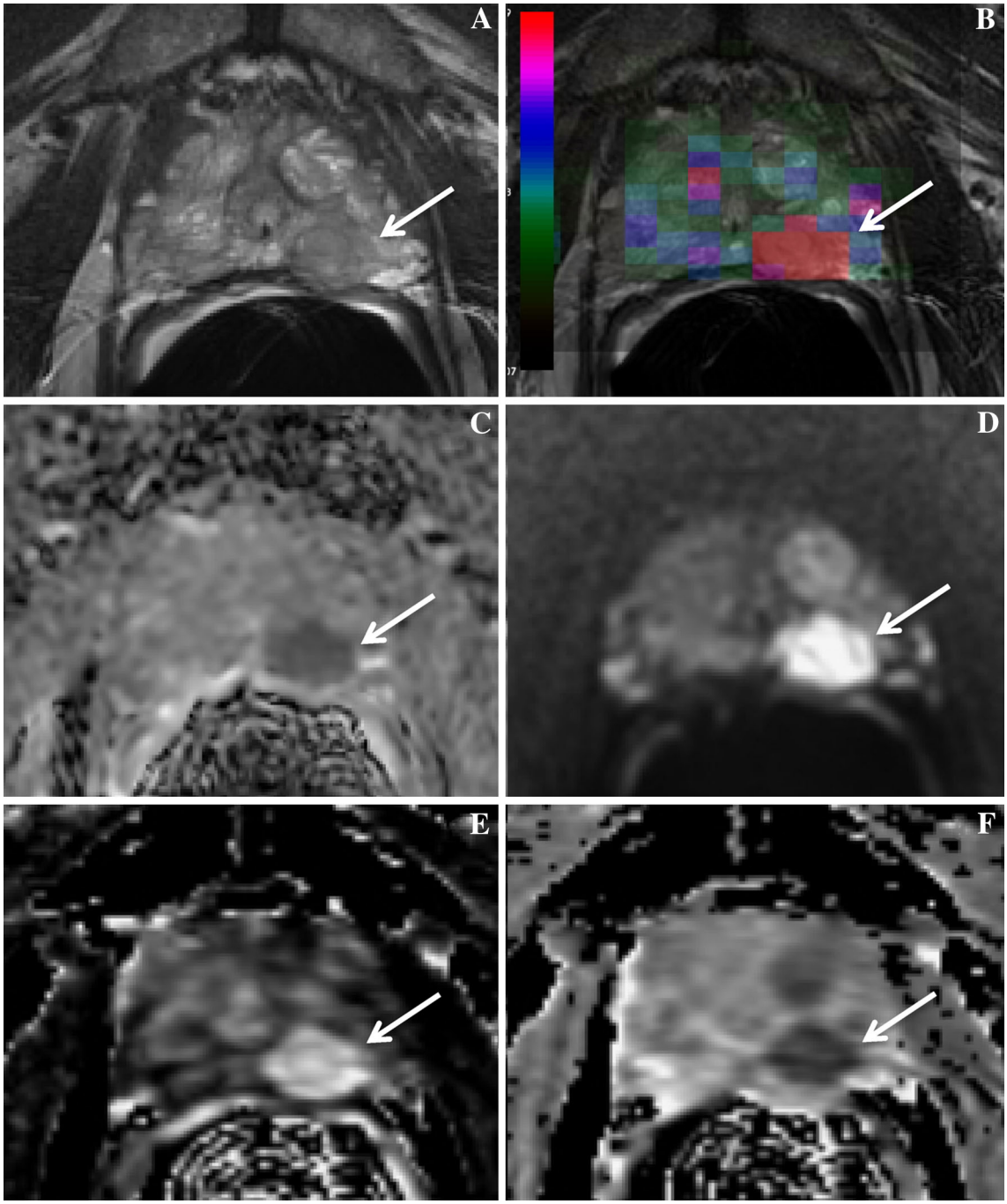

Fig. 1. An untreated 78-year-old man with serum PSA of 9.8 ng/ml showing a, **A** coil-corrected T2-weighted FSE image, **B** MRSI choline metabolite map created in SIVIC [94], **C** rFOV ADC map (b = 0, 600 s/mm^2), **D** coil-corrected rFOV DWI (b = 0, 1350 s/mm^2), and DCE-derived semi-quantitative parameters of **E** enhancement slope, and **F** washout slope. Subsequent TRUS–MRI fusion-guided biopsy revealed a Gleason 4 + 3 lesion in the left apex. Cancer regions are indicated by the *arrows*.

significant artifact on DWI and 1H-MRSI, and confound results from DCE MR imaging. For this reason, an interval of at least 6 weeks between the most recent prostate biopsy and the MRI scan is recommended [49, 50]. In addition, these T1-weighted images offer an opportunity to detect osseous metastases. While lesions will be incompletely assessed with a single sequence, after correlation with clinical history and histology, further diagnostic steps may be taken.

T2-weighted MR imaging

Multiplanar high-resolution two-dimensional (2D) fast spin-echo (FSE) T2-weighted MR images provide ex-

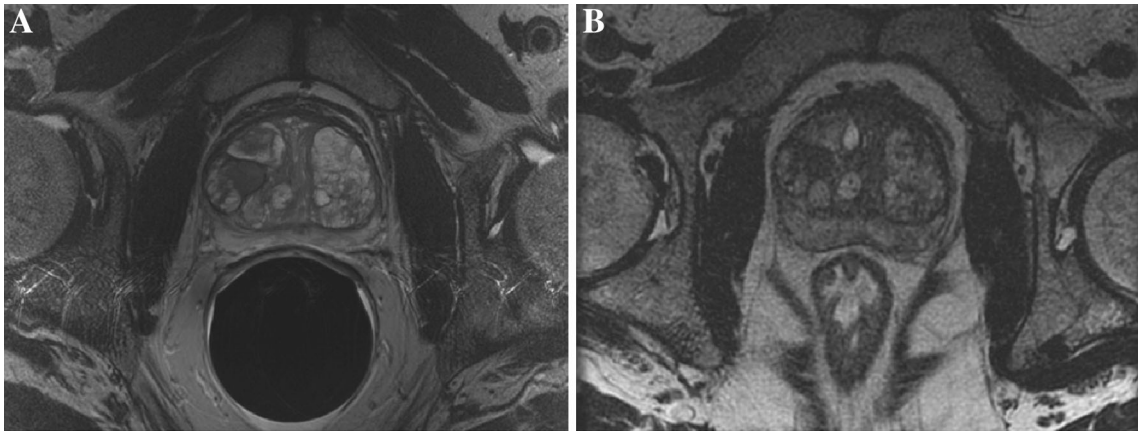

Fig. 2. An untreated 66-year-old man with no prior biopsies and serum PSA of 7.9 ng/ml. Oblique axial 2D FSE T2-weighted images acquired with 0.35 × 0.35 × 3 mm resolution, **A** with an endorectal coil and **B** without an endorectal coil. This patient was scanned twice in 3 months in anticipation of the MR-guided biopsy. We observe a noticeably increased noise in the image without an ERC, as well as diminished delineation between nodules inside the gland.

Table 1. Suggested acquisition parameters for the multiparametric MRI of the prostate with ERC

Series	PSD	Scan plane	TR (ms)	TE (ms)	Slice/Gap (mm)	FOV (mm)	Acquisition matrix	NEX	Sequence specific
Scout	FSE	3-plane	867	83	5/1.5	400 × 400	256 × 192	1	
T1	FGRE	Axial	5.06	2.46	4.2/0	240 × 240	192 × 128	1	3D
T2	FSE	Oblique axial	5000	96	3/0	180 × 180	256 × 256	3	2D
T2	FSE/CUBE	Oblique axial	2400	142.5	1.6/0	180 × 180	256 × 224	1	3D reformatting recommended
DWI mid	ss-EPI	Oblique axial	4725	Min	3/0	180 × 180	128 × 64	6	b = 600 s/mm^2 rFOV recommended
DWI high	ss-EPI	Oblique axial	4725	Min	3/0	260 × 260	128 × 64	7	b = 1350 s/mm^2
MRSI	3D PRESS	Oblique axial	2000	85	6/0	86.4 × 64.8 × 60	16 × 12 × 10	1	EPSI flyback
DCE	3D SPGR	Oblique axial	Min	Min	3/0	260 × 260	192 × 128	1	Temporal resolution = 10.4 s

Table 2. Suggested acquisition parameters for the multiparametric MRI of the prostate without ERC

Series	PSD	Scan plane	TR (ms)	TE (ms)	Slice/Gap (mm)	FOV (mm)	Acquisition matrix	NEX	Sequence specific
Scout	FSE	3-plane	867	83	5/1.5	400 × 400	256 × 192	1	
T1	FGRE	axial	5.06	In Phase	5/0	240 × 240	192 × 128	2	3D
T2	FSE	Oblique axial	6000	102	3/0	180 × 180	256 × 256	4	2D
T2	FSE	Oblique Coronal	5000	Min	3/0	180 × 180	256 × 256	4	2D
T2	FSE	Sagittal	5000	Min	3/0	180 × 180	192 × 192	2	2D
DWI mid	ss-EPI	Oblique axial	4000	Min	3/0	280 × 280	128 × 64	6	b = 800 s/mm^2
DCE	3D SPGR	Oblique axial	Min	Min	3/0	260 × 260	192 × 128	1	Temporal resolution = 10.4 s

quisite soft-tissue contrast and excellent depiction of zonal anatomy, and are the backbone of MR imaging of the prostate. The majority of prostate cancers are adenocarcinomas that arise within the peripheral zone. Most have low signal intensity against the background of the bright peripheral zone tissue. Transitional zone tumors represent most of the remaining prostate cancers. Similarly to peripheral zone cancers, these lesions usually have low signal intensity on T2-weighted MR images but can be difficult to distinguish from benign tissue, in particular in the presence of benign prostatic hyperplasia (BPH). T2-weighted MR imaging is also the main sequence utilized to assess locoregional spread of cancer [51, 52]; the diagnostic accuracy, though, is higher when it is combined with other functional sequences [53]. Prognosis, management, and treatment options of prostate cancer are greatly affected by cancer stage, in particular by the presence of extracapsular extension (ECE) and/or seminal vesicle invasion (SVI).

High-resolution 2D FSE T2-weighted images are acquired in the true sagittal plane, as well as the oblique axial (Fig. 1A) and oblique coronal planes of the prostate [54]. It is recommended that the slice thickness should not be more than 3 mm, without a gap, and the in-plane dimension of ≤0.7 mm (phase) $x \leq 0.4$ mm (frequency). For most patients, a field-of-view of 12–18 cm will allow for the inclusion of the entire gland and seminal vesicles. High-resolution 3D FSE T2-weighted MR imaging has emerged as a promising technique that allows for the acquisition of isotropic images and may

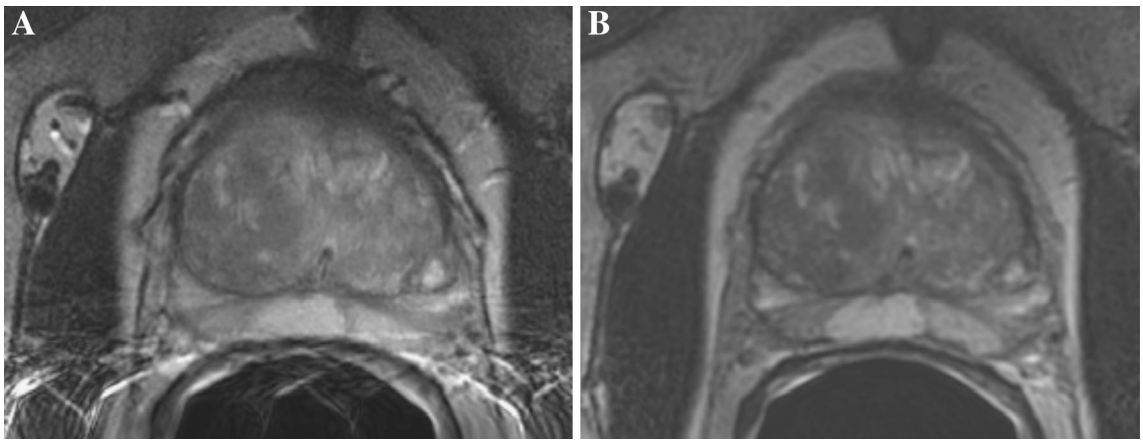

Fig. 3. An untreated 61-year-old man with biopsied Gleason 3 + 3 prostate cancer and serum PSA of 5.6 ng/ml showing an oblique axial, **A** T2-weighted FSE anatomic image and **B** T2-weighted 3D FSE anatomic image. The phase-encoding direction aliasing artifact present in the FSE image is not present in the CUBE image. However, the 3D FSE image has less contrast in comparison to the 2D FSE.

save time by reducing the number of sequences that need to be obtained. However, the quality of the 3D sequence may be limited if acquired on older or low-field magnets due to the need for thinly sliced images for adequate reformatting. While the T2 contrast is not the same as seen in 2D acquisitions, it is clinically acceptable [55]. Data of a study by Westphalen et al. showed that the preference for the 2D or 3D FSE MR images varies widely among radiologists, but without differences in their ability to delineate the anatomy and identify cancer [56]. This same study did find differences in image sharpness and the presence of some artifacts. The 2D FSE images were sharper than the 3D ones but demonstrated more artifacts (Fig. 3).

Diffusion-weighted MR imaging

DWI exploits the random motion of water molecules in biological tissues (Brownian motion) to characterize disease. These images are primarily utilized to calculate ADC maps (Fig. 1C). The glandular structure of the normal peripheral zone of the prostate compared to the shrunken glands or tightly packed cancerous tissue defines a well-established contrast between healthy and tumor tissue on DWI and the corresponding ADC maps [57]. Perhaps not surprisingly, DWI has been shown to increase the sensitivity and specificity of multiparametric MR imaging for the detection of prostate cancer [58–60]. It has also been shown to improve the assessment of tumor aggressiveness when combined with conventional T2-weighted imaging, with an inverse relationship between the apparent diffusion coefficient (ADC) map intensity and the Gleason score [61]. A threshold of approximately 850×10^{-6} mm^2/s has been used to distinguish between low- and high-grade tumors [62]. Yet, because of substantial overlap of ADC values seen in BPH and cancers, and variability across the various imaging platforms and due to different acquisition parameters, a qualitative visual assessment may be preferred.

Adequate characterization of the random motion of water requires information about its movement in multiple directions. Accordingly, DWI usually comprised at least three separate acquisitions, each measuring diffusion in a different direction. Due to this unique sequence structure, DWI is particularly prone to artifact from patient motion between directional acquisitions. To mitigate this problem, images are usually acquired with an echo-planar imaging (EPI) pulse sequence, designed to decrease scan time.

For prostate cancer detection on 3T scanners, the b-values are generally divided into mid (between 500 and 800 s/mm^2) and high (between 1000 and 2500 s/mm^2) (Fig. 1D) [63, 64]. Scanning on older magnets usually excludes b-values above 1000 s/mm^2 due to limits in gradient hardware. Using a lower b-value emphasizes extracellular effects in the resulting ADC maps, whereas using a high b-value emphasizes intracellular motion. Recently, it has become popular to utilize more than one b-value for the assessment of prostate cancer. Imaging with a mid-range b-value will normally have a greater SNR, which can result in finer resolution and a decreased number of signal averages per image. However, a high b-value acquisition reduces the signal from normal prostatic tissue, increasing the sensitivity to abnormal cellular environments [65]. One method of gaining the advantage of contrast of a high b-value while still having the high SNR and fine resolution of a lower b-value acquisition is to extrapolate and compute the theoretical image output for higher b-values [66]. These images show higher SNR than traditional DWI collected with the equivalent high b-values and can be utilized on older

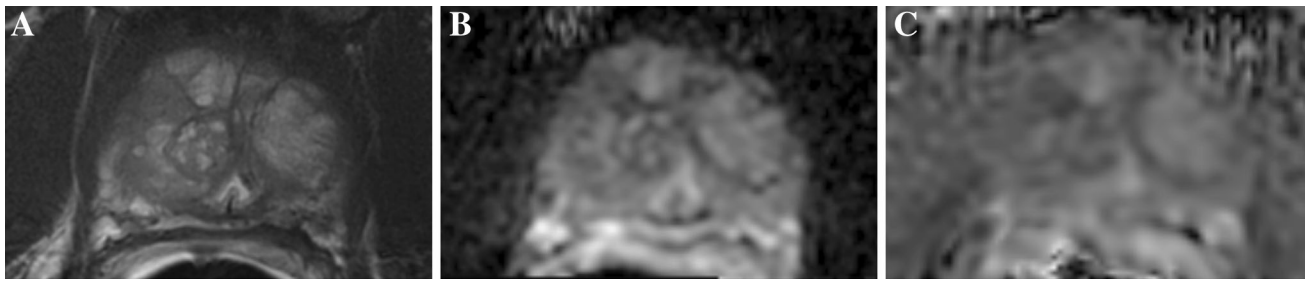

Fig. 4. An untreated 74-year-old man with biopsied Gleason 3 + 3 prostate cancer and serum PSA of 6.85 ng/ml. An oblique axial **A** T2-weighted 2D FSE anatomic image, **B** rFOV ADC map, and **C** full FOV ADC map show the advantages of the rFOV method for distinguishing boundaries of the prostate and BPH nodules within the prostate. We also see susceptibility artifact from fecal matter or air in the rectum, which significantly blurs the rectal wall on (**C**) and less so on (**B**).

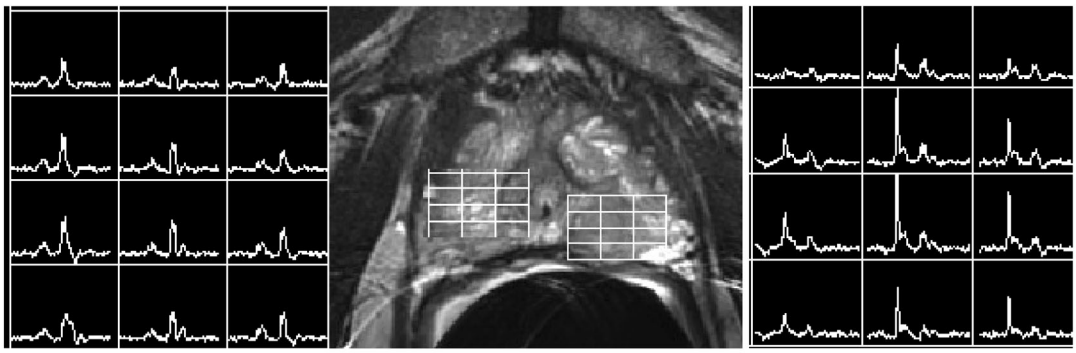

Fig. 5. An untreated 78-year-old man with serum PSA of 9.8 ng/ml. MRSI demonstrating highly elevated choline (*right panel*) in the *left apex*, drastically different from the contralateral healthy tissues (*left panel*) that demonstrate the presence of citrate without elevated choline. Subsequent TRUS–MRI fusion-guided biopsy revealed a Gleason 4 + 3 lesion in the *left apex*.

1.5T scanners where gradient hardware may not allow acquisition with high b-values [67].

In addition to more heavily diffusion-weighted images, a low b-value image is acquired with a *b*-value in the range of 0–100 s/mm^2 [68]. This image serves as a reference, to fit a slope to the signal per b-value per direction, which is combined to define the ADC map. The lower b-values are also used because they remove the effect of perfusion on the resulting ADC map.

In order to easily associate structural T2-weighted images with functional DWI data, DWI should be performed with the same or similar slice thickness and acquisition prescription to high-resolution T2-weighed imaging. DWI can be performed immediately after T2-weighted imaging to increase structural similarity.

DWI is heavily affected by susceptibility artifacts, which increase in magnitude with higher field strength [69]. Images acquired with EPI, in particular, suffer from severe susceptibility artifact at the interfaces of tissue with air, blood, or fecal matter in the rectum. These artifacts are important because they present at the border of the rectum and affect the peripheral zone of the prostate, where 70% of cancers are located [70]. Performing a rectal enema before the exam reduces susceptibility artifact from air or fecal matter in the rectum [71, 72]. A promising recent development for artifact reduction is reduced field-of-view imaging, which has been shown to improve image quality and contrast between tumor and healthy tissue, as well as to decrease susceptibility artifact in prostate DWI [73] (Fig. 4).

Two novel methods that may improve the characterization of prostate cancer are diffusion kurtosis (DK), which examines non-Gaussian water behavior at high b-values [74], and whole-lesion histogram analysis, which samples every voxel within a 3D region of interest [75]. While initial studies are promising, both require dedicated post-processing software for analysis and are currently exploratory techniques not suitable for use at most clinical sites (Fig. 5).

Dynamic contrast-enhanced imaging

Dynamic contrast-enhanced imaging follows the time course of tissue enhancement post contrast agent injec-

tion to evaluate the properties of tissue microstructure and neovascularity. Prostate cancer brings about changes in the cellular structure of the tissues, which result in altered interactions of the tissues with the injected contrast. It is believed that MR contrast agents do not reach the lumen of the healthy glandular tissues [76, 77]. Conversely, prostate cancer is marked by the loss of the basement membrane outside the glandular epithelial cells, which allows the contrast to enter the glands, resulting in a greater and faster tissue enhancement seen in DCE studies. In addition to continuing alterations in tissue microstructure, prostate cancer progression is also associated with neoangiogenesis [78–82]. The rapid growth and division of tumor vasculature result in disorganized, irregularly shaped, immature vessels [83–85]. DCE takes advantage of the unique characteristics associated with the abnormal tumor vasculature to assess aggressiveness of the disease. The usefulness of DCE in detecting, localizing, and staging prostate cancer is well documented in literature [58, 86–90]. Additionally, several studies have reported promising findings on the utility of DCE parameters in discriminating prostate cancer based on aggressiveness of the disease [91, 92]. While DCE is an invaluable sequence in certain instances where other acquisition sequences will show artifact (i.e., for patients with hip replacements), DCE results might be confounded by the presence of prostatitis in the peripheral zone [1, 5, 93] or by mixed BPH nodules in the central gland [1, 5, 94, 95].

DCE imaging is often done with a 3D Fast Spoiled Gradient Echo (3D-FSPGR) pulse sequence. T1-weighted images are collected before, during, and after administration of a contrast agent. A DCE scan is often preceded by a T1 mapping, a measurement of the native tissue relaxation time (T10) obtained using a series of volume acquisitions with variable flip angle values. Once the native T1 mapping is complete, several pre-contrast dynamic T1-weighted volumes are acquired to establish a baseline. The contrast agent is administered as an intravenous bolus at a rate of 2-4 ml/s followed by a 20-ml saline flush using a power injector. To ensure patient safety, patient's kidney function should be evaluated prior to contrast injection. Estimated glomerular filtration rate (eGFR) based on the blood creatinine levels are often used as indicators of kidney health. Once injected, the contrast agent does not penetrate the healthy prostate glands but collects in the extravascular extracellular space (EES), where it serves to shorten local relaxation times, producing high signal intensity on T1-weighted images. The contrast is cleared from the blood via renal excretion.

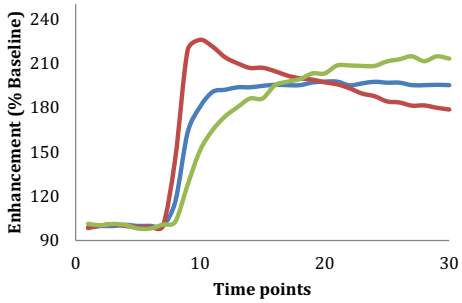

Fig. 6. Three main types of overall enhancement seen in prostate tissues: persistent enhancement, typically indicative of benign pathology (*green*); plateau, slightly suspicious for malignancy (*blue*); and washout, strongly suspicious for malignancy (*red*).

DCE-MRI studies typically utilize weight-adjusted (0.1 mmol/kg of body weight) paramagnetic gadolinium chelate contrast agents. There are several agents approved by the United States Food and Drug Administration, including gadopentetate dimeglumine (Magnevist), gadobutrol (Gadovist), or gadodiamide (Omniscan) [96]. Aiming for a reasonable spatiotemporal resolution, a five-minute DCE acquisition yields dynamic imaging with a temporal resolution in the range of 3–10 s, a spatial resolution in the range of 0.7 × 0.7 mm to 1.9 × 1.9 mm with a slice thickness of 3–4 mm [27, 66, 91, 92, 95, 97–101]. Compressed sensing techniques have been implemented into DCE sequences to improve spatiotemporal resolution or increase the coverage. Recently, Rosenkrantz et al. reported the use of a high-spatiotemporal resolution DCE technique GRASP (Golden-angle Radial Sparse Parallel), which allows for image acquisition with spatial resolution of 1.1 × 1.1 × 3.0 mm and temporal resolution of 2.3 s [102].

Tissue enhancement observed during DCE can be interpreted either by visually inspecting the raw images (qualitative approach) or by using semi-quantitative or quantitative methods [103–106]. The qualitative analysis of the DCE images [107–109] is based on the premise that the blood vessels recruited by the prostate tumors are leaky [110, 111]. When the contrast is injected, the cancerous tissues demonstrate early and rapid enhancement followed by a quick washout, which is noticeably different from a slow and steady enhancement observed for normal tissues. An observer may evaluate regions of interest within the prostate by categorizing the overall enhancement as 1) persistent—a steady enhancement, usually indicative of benign pathology, 2) plateau—the initial uptake is followed by a constant enhancement, slightly suspicious for malignancy, and 3) washout—a sharp uptake is followed by a steep washout, strongly suspicion for malignancy (Fig. 6). While the qualitative approach is quick and intuitive, it fails to comprehensively assess heterogeneous tissues and is inherently subjective and difficult to standardize among imaging centers.

Semi-quantitative analysis characterizes the enhancement curve on a voxel by voxel basis by calculating curve parameters such as maximum enhancement slope (Fig. 1E), time to peak, peak enhancement, washout slope (Fig. 1F), and area under the curve [92, 112]. Although this approach is extensively used in the assessment of DCE-MRI, the semi-quantitative parameters provide little physiologic insight into behavior of the tumor vessels and the usefulness of the computed metrics can be limited when comparing data across different imaging protocols. Normalization to muscle has been suggested to aid in generalization of semi-quantitative parameters [76].

The final approach to analyzing DCE images aims to estimate physiologically interpretable, kinetic parameters by fitting pharmacokinetic models to the enhancement curves [88, 113, 114]. The most common is the two-compartment model. The two compartments are the plasma space of the vasculature and the interstitial space between the prostate cells. The two main parameters derived from such models are K^{trans} (the volume transfer constant between plasma and extracellular space, expressed in units of min^{-1}) and v_e (the fractional volume of extracellular space per unit volume of tissue) [90, 115–118]. While K^{trans} maps offer diagnostically valuable information, acquiring stable measurements from quantitative analysis remains a challenge. Quantitative methods are affected by a number of variables such as changes in cardiac output, accurate tissue T1, and arterial input function (AIF) measurements, as well as the underlying assumptions made by the software packages. Accuracy of T1 measurements is greatly aided by T1 mapping [119]. Ideally, the AIF (the concentration of the contrast agent in the feeding blood supply) is measured for each individual patient in the femoral artery [120–122]. Unfortunately, in a clinical setting, the required temporal resolution may be difficult to achieve. A common approach is to use a population-averaged AIF in the form of a bi-exponential decay [97]. Finally, there are several open-source and commercially available software packages for both clinical and preclinical quantitative DCE analyses [123–127]. However, a few studies have been done to assess reproducibility of pharmacokinetic measurements obtained with different software packages.

The recently released second version of PI-RADS highlights the fact that DCE-MRI can be and is most widely assessed based on direct visualization of the raw data; optional tools, e.g., parametric maps and compartmental models, can be used to assist in diagnosis, but findings should always be confirmed on source images [3]. Last but not least, PI-RADS v2 characterizes a positive finding on DCE-MRI as a lesion with focal enhancement, earlier or contemporaneous with enhancement of adjacent normal tissues, and that corresponds to a suspicious finding on T2- or diffusion-weighted MR images.

Proton magnetic resonance spectroscopic imaging

Proton magnetic resonance spectroscopic imaging is a technique used to study in vivo cellular metabolism and has been established as a powerful technique for assessing patients with prostate cancer. Benign and malignant tissues can be differentiated based on the metabolic changes associated with prostate cancer [128, 129]. Normal prostatic glandular epithelial cells produce and secrete high levels of citrate (2.5–2.7 ppm) [130, 131]. Prostate cancer disrupts the epithelial tissues and triggers a metabolic shift from citrate production to citrate oxidation; the overall effect is a substantial reduction in citrate levels in malignant prostate tissues [132–134] (Fig. 5). Furthermore, increased cell density and elevated cell membrane turnover lead to increased levels of choline (3.21 ppm) in prostate cancer [135–137] (Fig. 1B). Creatine (3.02 ppm) is another metabolite of interest; it is maintained at a relatively constant level in both healthy and malignant prostatic tissues and serves as an internal Ref. [134]. Lastly, some groups found it informative to track metabolic changes associated with polyamine [129]. Polyamines (especially spermine) are found in healthy prostate epithelial cells, and similar to citrate, their levels are dramatically reduced in prostate cancer [138].

Due to the multifocal nature of prostate cancer, a high-resolution metabolic mapping of the entire prostate is required for accurate cancer localization and diagnosis. The 1H-MRSI acquisition has evolved from single-voxel spectroscopy to 3D 1H-MRSI that is typically acquired using phase encoding in all three directions but is time consuming. Improvements in pulse sequence design have enabled the acquisition of metabolic information from the entire prostate at high resolution within less than 10 min with voxel sizes ranging from 0.2 to 0.5 cm^3, making 1H-MRSI a clinically feasible technique [139, 140]. These include using flyback echo-planar readout gradients to improve efficiency and robustness to errors and non-uniform undersampling, and compressed sensing to accelerate the acquisition [141, 142]. A number of techniques have been used to reduce the negative effects of periprostatic fat, including outer volume saturation (OVS) with very selective suppression (VSS) pulses [143], band selective inversion with gradient dephasing (BASING) [144, 145], and spectral-spatial radiofrequency pulses [146, 147].

The 1H-MRSI sequence is usually prescribed off the axial T2-weighted MR images with a volume selected to maximally cover the prostate while excluding the seminal vesicles, periprostatic fat, and as much of the rectum as possible. Standard post-processing involves zero-filling, apodization using Gaussian or Lorentzian filtering, and Fourier transform of the free induction decay signal, as well as baseline and phase corrections [148–151].

Interpretation of 1H-MRSI data is often done on a voxel-by-voxel basis, which can be time consuming and introduce interobserver variability. An alternative approach to review these metabolites is to observe peak area ratios, such as the choline + creatine to citrate ratio within each voxel: choline and creatine are typically combined due to signal overlap. In 2004, Jung et al. proposed a standardized scoring system for peripheral zone tissues based on metabolic data, ranging from 1 (definitely normal) to 5 (definitely cancer) [152]. And in 2007, Futterer et al. introduced standardized thresholds for differentiation of benign and malignant tissues in the peripheral zone and central gland of the prostate [153]. Several studies reported significant correlations between peak area ratios and Gleason scores [154, 155]; yet, interpretation can be hindered by choline contamination from the seminal vesicles or urethra [134, 156] or by prostatitis [157, 158], which can result in false positive findings.

It is also important to note that the data of some studies were unfavorable to the clinical usefulness of 1H-MRSI, more notoriously those of the ACRIN 6659 study published by Weinreb et al. that found no incremental benefit for 1H-MRSI compared with MRI alone in sextant tumor localization [29]. Based on such data, and possibly on the complexity of imaging acquisition and interpretation, 1H-MRSI, which was an optional tool in the initial version of PI-RADS, no longer influences the assessment of lesion in PI-RADS v2.

Patient preparation

We have anecdotally noted that providing patients with information detailing the procedure and the required preparation prior to the exam improves patient compliance. Patients with severe claustrophobia may be required or advised to bring prescription sedatives to the exam. In some centers, antispasmodic agents like butylscopolamine are administered immediately prior to scanning to decrease bowel peristalsis and potential artifacts related to motion. However, peristaltic suppression is controversial, as some groups have failed to identify a significant improvement of image quality in studies performed on 3T scanner without an ERC [159–161]. Patients undergoing scans with an ERC should be advised to perform a saline laxative enema within a 3-h window of the exam to facilitate proper endorectal coil placement and minimize susceptibility artifacts associated with air or fecal contamination. Enemas are not required prior to scans done without an ERC, though, as the improvement in image quality is at best marginal [162]. Some imaging facilities also recommend patients to abstain from ejaculating 1–3 days prior to the MR scan in order to maintain distention of the seminal vesicles and increase conspicuity of possible tumor invasion. The validity of this claim, however, has not been tested. In a pilot study, Medved et al. reported decreased signal intensity on T2-weighted imaging and the apparent diffusion coefficient maps in the peripheral zone after ejaculation, possibly reflecting a reduction in the volume of ejaculatory fluid within the gland [163]. The authors did not observe any dramatic differences in image quality or significant changes in prostate volume after ejaculation. Since the study was done in healthy volunteers, the effect of ejaculation on prostate cancer diagnosis has not been established.

Conclusion

Use of mpMRI exams for the diagnosis and staging of prostate cancer has become prominent at medical centers around the world [164–166] and is likely to continue expanding into increasing modalities in the age of precision medicine. However, mpMRI of the prostate did not yet gain the same level of acceptance of other imaging tests; and this is at least in part due to the use of suboptimal protocols, lack of standardization, and inadequate patient preparation. The American College of Radiology, in conjunction with the European Society of Urogenital Radiology and the AdMeTech Foundation, has developed standards for the Prostate Imaging Reporting and Data System (PI-RADS) [3]. Currently, in its version number 2, in addition to providing guidelines for interpretation and reporting of mpMRI, PI-RADS establishes the minimum acceptable technical parameters for scanning patients. Finally, regardless of the magnet strength, the use of an endorectal coil, or the details of the imaging protocol, patient preparation is essential to acquiring the highest quality images while maintaining maximal patient comfort and compliance. Equally important in providing the best imaging exam for patient diagnosis is the communication between primary physicians, radiologists, researchers, and staff.

Acknowledgments. This work was in part supported by the grant NIH RO1 CA148708 (PI Noworolski).

References

1. Barentsz JO, Richenberg J, Clements R, et al. (2012) ESUR prostate MR guidelines 2012. Eur Radiol 22(4):746–757. doi:10.1007/s00330-011-2377-y
2. Dickinson L, Ahmed HU, Allen C, et al. (2013) Scoring systems used for the interpretation and reporting of multiparametric MRI for prostate cancer detection, localization, and characterization: could standardization lead to improved utilization of imaging within the diagnostic pathway? J Magn Reson Imaging 37(1):48–58. doi:10.1002/jmri.23689
3. ACR (2015) MR Prostate Imaging Reporting and Data System version 2.0. American College of Radiology. http://www.acr.org/Quality-Safety/Resources/PIRADS/. Accessed 16 April 2015
4. Fenner A (2013) Prostate cancer: multiparametric MRI scans could be a useful adjunct for active surveillance in prostate cancer. Nat Rev Urol 10(5):247. doi:10.1038/nrurol.2013.56
5. Hoeks CM, Barentsz JO, Hambrock T, et al. (2011) Prostate cancer: multiparametric MR imaging for detection, localization, and staging. Radiology 261(1):46–66. doi:10.1148/radiol.11091822

6. Johnson LM, Turkbey B, Figg WD, Choyke PL (2014) Multiparametric MRI in prostate cancer management. Nat Rev Clin Oncol 11(6):346–353. doi:10.1038/nrclinonc.2014.69
7. Kurhanewicz J, Vigneron D, Carroll P, Coakley F (2008) Multiparametric magnetic resonance imaging in prostate cancer: present and future. Curr Opin Urol 18(1):71–77. doi:10.1097/MOU.0b013e3282f19d01
8. Sandler K, Patel M, Lynne C, et al. (2015) Multiparametric-MRI and targeted biopsies in the management of prostate cancer patients on active surveillance. Frontiers in Oncology 5:4. doi:10.3389/fonc.2015.00004
9. Rouviere O (2012) Imaging techniques for local recurrence of prostate cancer: for whom, why and how? Diagn Interv Imaging 93(4):279–290. doi:10.1016/j.diii.2012.01.012
10. Kim CK, Park BK, Lee HM (2009) Prediction of locally recurrent prostate cancer after radiation therapy: incremental value of 3T diffusion-weighted MRI. J Magn Reson Imaging 29(2):391–397. doi:10.1002/jmri.21645
11. Westphalen AC, Reed GD, Vinh PP, et al. (2012) Multiparametric 3T endorectal mri after external beam radiation therapy for prostate cancer. J Magn Reson Imaging 36(2):430–437. doi:10.1002/jmri.23672
12. Bubley GJ, Bloch BN, Vazquez C, et al. (2013) Accuracy of endorectal magnetic resonance/transrectal ultrasound fusion for detection of prostate cancer during brachytherapy. Urology 81(6):1284–1289. doi:10.1016/j.urology.2012.12.051
13. Barrett T, Gill AB, Kataoka MY, et al. (2012) DCE and DW MRI in monitoring response to androgen deprivation therapy in patients with prostate cancer: a feasibility study. Magn Reson Med 67(3):778–785. doi:10.1002/mrm.23062
14. Chen M, Hricak H, Kalbhen CL, et al. (1996) Hormonal ablation of prostatic cancer: effects on prostate morphology, tumor detection, and staging by endorectal coil MR imaging. Am J Roentgenol 166(5):1157–1163. doi:10.2214/ajr.166.5.8615261
15. Miralbell R, Vees H, Lozano J, et al. (2007) Endorectal MRI assessment of local relapse after surgery for prostate cancer: a model to define treatment field guidelines for adjuvant radiotherapy in patients at high risk for local failure. Int J Radiat Oncol Biol Phys 67(2):356–361. doi:10.1016/j.ijrobp.2006.08.079
16. Pucar D, Sella T, Schoder H (2008) The role of imaging in the detection of prostate cancer local recurrence after radiation therapy and surgery. Curr Opin Urol 18(1):87–97. doi:10.1097/MOU.0b013e3282f13ac3
17. Charnley N, Morgan A, Thomas E, et al. (2005) The use of CT-MR image registration to define target volumes in pelvic radiotherapy in the presence of bilateral hip replacements. Br J Radiol 78(931):634–636. doi:10.1259/bjr/28412864
18. Rosewall T, Kong V, Vesprini D, et al. (2009) Prostate delineation using CT and MRI for radiotherapy patients with bilateral hip prostheses. Radiother Oncol 90(3):325–330. doi:10.1016/j.radonc.2008.11.015
19. Rudisch A, Kremser C, Peer S, et al. (1998) Metallic artifacts in magnetic resonance imaging of patients with spinal fusion. A comparison of implant materials and imaging sequences. Spine 23(6):692–699
20. Panfili E, Pierdicca L, Salvolini L, et al. (2014) Magnetic resonance imaging (MRI) artefacts in hip prostheses: a comparison of different prosthetic compositions. Radiol Med 119(2):113–120. doi:10.1007/s11547-013-0315-6
21. Delongchamps NB, Beuvon F, Eiss D, et al. (2011) Multiparametric MRI is helpful to predict tumor focality, stage, and size in patients diagnosed with unilateral low-risk prostate cancer. Prostate Cancer Prostatic Dis 14(3):232–237. doi:10.1038/pcan.2011.9
22. Delongchamps NB, Rouanne M, Flam T, et al. (2011) Multiparametric magnetic resonance imaging for the detection and localization of prostate cancer: combination of T2-weighted, dynamic contrast-enhanced and diffusion-weighted imaging. BJU Int 107(9):1411–1418. doi:10.1111/j.1464-410X.2010.09808.x
23. Franiel T, Stephan C, Erbersdobler A, et al. (2011) Areas suspicious for prostate cancer: MR-guided biopsy in patients with at least one transrectal US-guided biopsy with a negative finding–multiparametric MR imaging for detection and biopsy planning. Radiology 259(1):162–172. doi:10.1148/radiol.10101251
24. Futterer JJ, Heijmink SW, Scheenen TW, et al. (2006) Prostate cancer localization with dynamic contrast-enhanced MR imaging and proton MR spectroscopic imaging. Radiology 241(2):449–458
25. Haider MA, van der Kwast TH, Tanguay J, et al. (2007) Combined T2-weighted and diffusion-weighted MRI for localization of prostate cancer. Am J Roentgenol 189(2):323–328. doi:10.2214/AJR.07.2211
26. Langer DL, van der Kwast TH, Evans AJ, et al. (2010) Prostate tissue composition and MR measurements: investigating the relationships between ADC, T2, K(trans), v(e), and corresponding histologic features. Radiology 255(2):485–494. doi:10.1148/radiol.10091343
27. Langer DL, van der Kwast TH, Evans AJ, et al. (2009) Prostate cancer detection with multi-parametric MRI: logistic regression analysis of quantitative T2, diffusion-weighted imaging, and dynamic contrast-enhanced MRI. J Magn Reson Imaging 30(2):327–334. doi:10.1002/jmri.21824
28. Mazaheri Y, Hricak H, Fine SW, et al. (2009) Prostate tumor volume measurement with combined T2-weighted imaging and diffusion-weighted MR: correlation with pathologic tumor volume. Radiology 252(2):449–457. doi:10.1148/radiol.2523081423
29. Weinreb JC, Blume JD, Coakley FV, et al. (2009) Prostate cancer: sextant localization at MR imaging and MR spectroscopic imaging before prostatectomy–results of ACRIN prospective multi-institutional clinicopathologic study. Radiology 251(1):122–133. doi:10.1148/radiol.2511080409
30. Hricak H, Choyke PL, Eberhardt SC, Leibel SA, Scardino PT (2007) Imaging prostate cancer: a multidisciplinary perspective. Radiology 243(1):28–53. doi:10.1148/radiol.2431030580
31. Noworolski SM, Crane JC, Vigneron DB, Kurhanewicz J (2008) A clinical comparison of rigid and inflatable endorectal-coil probes for MRI and 3D MR spectroscopic imaging (MRSI) of the prostate. J Magn Reson Imaging 27(5):1077–1082. doi:10.1002/jmri.21331
32. Eilenberg SS, Tartar VM, Mattrey RF (1994) Reducing magnetic susceptibility differences using liquid fluorocarbon pads (Sat Pad): results with spectral presaturation of fat. Artif Cells Blood Substit Immobil Biotechnol 22(4):1477–1483
33. Rosen Y, Bloch BN, Lenkinski RE, et al. (2007) 3T MR of the prostate: reducing susceptibility gradients by inflating the endorectal coil with a barium sulfate suspension. Magn Reson Med 57(5):898–904. doi:10.1002/mrm.21166
34. Noworolski SM, Reed GD, Kurhanewicz J, Vigneron DB (2010) Post-processing correction of the endorectal coil reception effects in MR spectroscopic imaging of the prostate. J Magn Reson Imaging 32(3):654–662. doi:10.1002/jmri.22258
35. Bloch BN, Rofsky NM, Baroni RH, et al. (2004) 3 Tesla magnetic resonance imaging of the prostate with combined pelvic phased-array and endorectal coils: initial experience(1). Acad Radiol 11(8): 863–867. doi:10.1016/j.acra.2004.04.017
36. Chang KJ, Kamel IR, Macura KJ, Bluemke DA (2008) 3.0-T MR imaging of the abdomen: comparison with 1.5 T. Radiographics 28(7):1983–1998. doi:10.1148/rg.287075154
37. Park BK, Kim B, Kim CK, Lee HM, Kwon GY (2007) Comparison of Phased-Array 3.0-T and Endorectal 1.5-T magnetic resonance imaging in the evaluation of local staging accuracy for prostate cancer. J Comput Assist Tomogr 31(4):534–538
38. Shah ZK, Elias SN, Abaza R, et al. (2015) Performance comparison of 1.5-T endorectal coil MRI with 3.0-T nonendorectal coil MRI in patients with prostate cancer. Acad Radiol 22(4):467–474. doi:10.1016/j.acra.2014.11.007
39. Sosna J, Pedrosa I, Dewolf WC, et al. (2004) MR imaging of the prostate at 3 Tesla: comparison of an external phased-array coil to imaging with an endorectal coil at 1.5 Tesla. Acad Radiol 11(8): 857–862
40. Turkbey B, Merino MJ, Gallardo EC, et al. (2014) Comparison of endorectal coil and nonendorectal coil T2 W and diffusion-weighted MRI at 3 Tesla for localizing prostate cancer: correlation with whole-mount histopathology. J Magn Reson Imaging 39(6): 1443–1448. doi:10.1002/jmri.24317
41. Litjens GJ, Barentsz JO, Karssemeijer N, Huisman HJ (2015) Clinical evaluation of a computer-aided diagnosis system for determining cancer aggressiveness in prostate MRI. Eur Radiol . doi:10.1007/s00330-015-3743-y

42. Silveira PC, Dunne R, Sainani NI, et al. (2015) Impact of an information technology-enabled initiative on the quality of prostate multiparametric MRI reports. Acad Radiol 22(7):827–833. doi:10.1016/j.acra.2015.02.018
43. Hambrock T, Vos PC, Hulsbergen-van de Kaa CA, Barentsz JO, Huisman HJ (2013) Prostate cancer: computer-aided diagnosis with multiparametric 3-T MR imaging–effect on observer performance. Radiology 266(2):521–530. doi:10.1148/radiol.12111634
44. Siddiqui MM, Rais-Bahrami S, Turkbey B, et al. (2015) Comparison of MR/ultrasound fusion-guided biopsy with ultrasound-guided biopsy for the diagnosis of prostate cancer. JAMA 313(4):390–397. doi:10.1001/jama.2014.17942
45. Vargas C, Saito AI, Hsi WC, et al. (2010) Cine-magnetic resonance imaging assessment of intrafraction motion for prostate cancer patients supine or prone with and without a rectal balloon. Am J Clin Oncol 33(1):11–16. doi:10.1097/COC.0b013e31819fdf7c
46. Wilder RB, Chittenden L, Mesa AV, et al. (2010) A prospective study of intrafraction prostate motion in the prone vs. supine position. Int J Radiat Oncol Biol Phys 77(1):165–170. doi:10.1016/j.ijrobp.2009.04.041
47. Pasoglou V, Michoux N, Peeters F, et al. (2015) Whole-body 3D T1-weighted MR imaging in patients with prostate cancer: feasibility and evaluation in screening for metastatic disease. Radiology 275(1):155–166. doi:10.1148/radiol.14141242
48. Pano B, Sebastia C, Bunesch L, et al. (2011) Pathways of lymphatic spread in male urogenital pelvic malignancies. Radiographics 31(1):135–160. doi:10.1148/rg.311105072
49. Qayyum A, Coakley FV, Lu Y, et al. (2004) Organ-confined prostate cancer: effect of prior transrectal biopsy on endorectal MRI and MR spectroscopic imaging. Am J Roentgenol 183(4):1079–1083. doi:10.2214/ajr.183.4.1831079
50. Sharif-Afshar AR, Feng T, Koopman S, et al. (2015) Impact of post prostate biopsy hemorrhage on multiparametric magnetic resonance imaging. Can J Urol 22(2):7698–7702
51. Sala E, Akin O, Moskowitz CS, et al. (2006) Endorectal MR imaging in the evaluation of seminal vesicle invasion: diagnostic accuracy and multivariate feature analysis. Radiology 238(3):929–937. doi:10.1148/radiol.2383050657
52. Tempany CM, Rahmouni AD, Epstein JI, Walsh PC, Zerhouni EA (1991) Invasion of the neurovascular bundle by prostate cancer: evaluation with MR imaging. Radiology 181(1):107–112
53. de Rooij M, Hamoen EH, Witjes JA, Barentsz JO, Rovers MM (2015) Accuracy of magnetic resonance imaging for local staging of prostate cancer: a diagnostic meta-analysis. Eur Urol . doi:10.1016/j.eururo.2015.07.029
54. Schiebler ML, Schnall MD, Pollack HM, et al. (1993) Current role of MR imaging in the staging of adenocarcinoma of the prostate. Radiology 189(2):339–352. doi:10.1148/radiology.189.2.8210358
55. Rosenkrantz AB, Neil J, Kong X, et al. (2010) Prostate cancer: comparison of 3D T2-weighted with conventional 2D T2-weighted imaging for image quality and tumor detection. Am J Roentgenol 194(2):446–452. doi:10.2214/AJR.09.3217
56. Westphalen AC, Noworolski S, Sen S et al (2015) Kurhanewicz J High resolution 3-Tesla endorectal prostate MR Imaging: a multireader study of radiologist preference and perceived interpretive quality of 2D and 3D T2-weighted FSE MR images (abstract #15001483). In: RSNA 101st Scientific Assembly and Annual Meeting, Chicago, Nov 28 to Dec 4, 2015. Radiological Society of North America
57. Desouza NM, Reinsberg SA, Scurr ED, Brewster JM, Payne GS (2007) Magnetic resonance imaging in prostate cancer: the value of apparent diffusion coefficients for identifying malignant nodules. Br J Radiol 80(950):90–95. doi:10.1259/bjr/24232319
58. Gibbs P, Pickles MD, Turnbull LW (2006) Diffusion imaging of the prostate at 3.0 tesla. Invest Radiol 41(2):185–188
59. Kim CK, Park BK, Lee HM, Kwon GY (2007) Value of diffusion-weighted imaging for the prediction of prostate cancer location at 3T using a phased-array coil: preliminary results. Invest Radiol 42(12):842–847. doi:10.1097/RLI.0b013e3181461d21
60. Turkbey B, Pinto PA, Choyke PL (2009) Imaging techniques for prostate cancer: implications for focal therapy. Nat Rev Urol 6(4):191–203. doi:10.1038/nrurol.2009.27
61. Vargas HA, Akin O, Franiel T, et al. (2011) Diffusion-weighted endorectal MR imaging at 3 T for prostate cancer: tumor detection and assessment of aggressiveness. Radiology 259(3):775–784. doi:10.1148/radiol.11102066
62. Nagarajan R, Margolis D, Raman S, et al. (2012) Correlation of Gleason scores with diffusion-weighted imaging findings of prostate cancer. Adv Urol 2012:374805. doi:10.1155/2012/374805
63. Pang Y, Turkbey B, Bernardo M, et al. (2013) Intravoxel incoherent motion MR imaging for prostate cancer: an evaluation of perfusion fraction and diffusion coefficient derived from different b-value combinations. Magn Reson Med 69(2):553–562. doi:10.1002/mrm.24277
64. Wang XZ, Wang B, Gao ZQ, et al. (2009) Diffusion-weighted imaging of prostate cancer: correlation between apparent diffusion coefficient values and tumor proliferation. J Magn Reson Imaging 29(6):1360–1366. doi:10.1002/jmri.21797
65. Katahira K, Takahara T, Kwee TC, et al. (2011) Ultra-high-b-value diffusion-weighted MR imaging for the detection of prostate cancer: evaluation in 201 cases with histopathological correlation. Eur Radiol 21(1):188–196. doi:10.1007/s00330-010-1883-7
66. Rosenkrantz AB, Sabach A, Babb JS, et al. (2013) Prostate cancer: comparison of dynamic contrast-enhanced MRI techniques for localization of peripheral zone tumor. Am J Roentgenol 201(3):W471–478. doi:10.2214/AJR.12.9737
67. Ueno Y, Takahashi S, Kitajima K, et al. (2013) Computed diffusion-weighted imaging using 3-T magnetic resonance imaging for prostate cancer diagnosis. Eur Radiol 23(12):3509–3516. doi:10.1007/s00330-013-2958-z
68. Thoeny HC, Ross BD (2010) Predicting and monitoring cancer treatment response with diffusion-weighted MRI. J Magn Reson Imaging 32(1):2–16. doi:10.1002/jmri.22167
69. Farahani K, Sinha U, Sinha S, Chiu LC, Lufkin RB (1990) Effect of field strength on susceptibility artifacts in magnetic resonance imaging. Comput Med Imaging Graph 14(6):409–413
70. Rickards D (1992) Transrectal ultrasound 1992. Br J Urol 69(5):449–455
71. Mazaheri Y, Vargas HA, Nyman G, et al. (2013) Diffusion-weighted MRI of the prostate at 3.0 T: comparison of endorectal coil (ERC) MRI and phased-array coil (PAC) MRI-The impact of SNR on ADC measurement. Eur J Radiol 82(10):e515–520. doi:10.1016/j.ejrad.2013.04.041
72. Metens T, Miranda D, Absil J, Matos C (2012) What is the optimal b value in diffusion-weighted MR imaging to depict prostate cancer at 3T? Eur Radiol 22(3):703–709. doi:10.1007/s00330-011-2298-9
73. Korn N, Kurhanewicz J, Banerjee S, et al. (2015) Reduced-FOV excitation decreases susceptibility artifact in diffusion-weighted MRI with endorectal coil for prostate cancer detection. Magn Reson Imaging 33(1):56–62. doi:10.1016/j.mri.2014.08.040
74. Quentin M, Pentang G, Schimmoller L, et al. (2014) Feasibility of diffusional kurtosis tensor imaging in prostate MRI for the assessment of prostate cancer: preliminary results. Magn Reson Imaging 32(7):880–885. doi:10.1016/j.mri.2014.04.005
75. Donati OF, Mazaheri Y, Afaq A, et al. (2014) Prostate cancer aggressiveness: assessment with whole-lesion histogram analysis of the apparent diffusion coefficient. Radiology 271(1):143–152. doi:10.1148/radiol.13130973
76. Noworolski SM, Henry RG, Vigneron DB, Kurhanewicz J (2005) Dynamic contrast-enhanced MRI in normal and abnormal prostate tissues as defined by biopsy, MRI, and 3D MRSI. Magn Reson Med 53(2):249–255. doi:10.1002/mrm.20374
77. Noworolski SM, Reed GD, Kurhanewicz J (2011) A novel luminal water model for DCE MRI of prostatic tissues. Paper presented at the proceedings of International Society Magnus Reason Medicine, 19 Montreal
78. Bergers G, Benjamin LE (2003) Tumorigenesis and the angiogenic switch. Nat Rev Cancer 3(6):401–410. doi:10.1038/nrc1093
79. Ferrer FA, Miller LJ, Andrawis RI, et al. (1997) Vascular endothelial growth factor (VEGF) expression in human prostate cancer: in situ and in vitro expression of VEGF by human prostate cancer cells. J Urol 157(6):2329–2333
80. Huss WJ, Hanrahan CF, Barrios RJ, Simons JW, Greenberg NM (2001) Angiogenesis and prostate cancer: identification of a molecular progression switch. Cancer Res 61(6):2736–2743
81. Latil A, Bieche I, Pesche S, et al. (2000) VEGF overexpression in clinically localized prostate tumors and neuropilin-1 overexpression in metastatic forms. Int J Cancer 89(2):167–171

82. Russo G, Mischi M, Scheepens W, De la Rosette JJ, Wijkstra H (2012) Angiogenesis in prostate cancer: onset, progression and imaging. BJU Int 110 (11 Pt C):E794-808. doi:10.1111/j.1464-410X.2012.11444.x
83. Bigler SA, Deering RE, Brawer MK (1993) Comparison of microscopic vascularity in benign and malignant prostate tissue. Hum Pathol 24(2):220–226
84. McDonald DM, Baluk P (2002) Significance of blood vessel leakiness in cancer. Cancer Res 62(18):5381–5385
85. Sottnik JL, Zhang J, Macoska JA, Keller ET (2011) The PCa tumor microenvironment. Cancer Microenviron 4(3):283–297. doi:10.1007/s12307-011-0073-8
86. Isebaert S, Van den Bergh L, Haustermans K, et al. (2013) Multiparametric MRI for prostate cancer localization in correlation to whole-mount histopathology. J Magn Reson Imaging 37(6):1392–1401. doi:10.1002/jmri.23938
87. Ito H, Kamoi K, Yokoyama K, Yamada K, Nishimura T (2003) Visualization of prostate cancer using dynamic contrast-enhanced MRI: comparison with transrectal power Doppler ultrasound. Br J Radiol 76(909):617–624. doi:10.1259/bjr/52526261
88. Jackson AS, Reinsberg SA, Sohaib SA, et al. (2009) Dynamic contrast-enhanced MRI for prostate cancer localization. Br J Radiol 82(974):148–156. doi:10.1259/bjr/89518905
89. Kim JK, Hong SS, Choi YJ, et al. (2005) Wash-in rate on the basis of dynamic contrast-enhanced MRI: usefulness for prostate cancer detection and localization. J Magn Reson Imaging 22(5):639–646. doi:10.1002/jmri.20431
90. Ocak I, Bernardo M, Metzger G, et al. (2007) Dynamic contrast-enhanced MRI of prostate cancer at 3 T: a study of pharmacokinetic parameters. Am J Roentgenol 189(4):849. doi:10.2214/AJR.06.1329
91. Chen YJ, Chu WC, Pu YS, et al. (2012) Washout gradient in dynamic contrast-enhanced MRI is associated with tumor aggressiveness of prostate cancer. J Magn Reson Imaging 36(4):912–919. doi:10.1002/jmri.23723
92. Vos EK, Litjens GJ, Kobus T, et al. (2013) Assessment of prostate cancer aggressiveness using dynamic contrast-enhanced magnetic resonance imaging at 3 T. Eur Urol 64(3):448–455. doi:10.1016/j.eururo.2013.05.045
93. Rosenkrantz AB, Taneja SS (2014) Radiologist, be aware: ten pitfalls that confound the interpretation of multiparametric prostate MRI. Am J Roentgenol 202(1):109–120. doi:10.2214/AJR.13.10699
94. Akin O, Sala E, Moskowitz CS, et al. (2006) Transition zone prostate cancers: features, detection, localization, and staging at endorectal MR imaging. Radiology 239(3):784–792
95. Hoeks CM, Hambrock T, Yakar D, et al. (2013) Transition zone prostate cancer: detection and localization with 3-T multiparametric MR imaging. Radiology 266(1):207–217. doi:10.1148/radiol.12120281
96. Kershaw LE, Buckley DL (2006) Precision in measurements of perfusion and microvascular permeability with T1-weighted dynamic contrast-enhanced MRI. Magn Reson Med 56(5):986–992. doi:10.1002/mrm.21040
97. Fennessy FM, Fedorov A, Penzkofer T, et al. (2015) Quantitative pharmacokinetic analysis of prostate cancer DCE-MRI at 3T: comparison of two arterial input functions on cancer detection with digitized whole mount histopathological validation. Magn Reson Imaging 33(7):886–894. doi:10.1016/j.mri.2015.02.008
98. Perdona S, Di Lorenzo G, Autorino R, et al. (2013) Combined magnetic resonance spectroscopy and dynamic contrast-enhanced imaging for prostate cancer detection. Urol Oncol 31(6):761–765. doi:10.1016/j.urolonc.2011.07.010
99. Quon J, Kielar AZ, Jain R, Schieda N (2015) Assessing the utilization of functional imaging in multiparametric prostate MRI in routine clinical practice. Clin Radiol 70(4):373–378. doi:10.1016/j.crad.2014.12.001
100. Turkbey B, Mani H, Aras O, et al. (2013) Prostate cancer: can multiparametric MR imaging help identify patients who are candidates for active surveillance? Radiology 268(1):144–152. doi:10.1148/radiol.13121325
101. Zhang X, Quan X, Lu S, et al. (2014) The clinical value of dynamic contrast-enhanced magnetic resonance imaging at 3.0T to detect prostate cancer. J Int Med Res 42(5):1077–1084. doi:10.1177/0300060514541827
102. Rosenkrantz AB, Geppert C, Grimm R, et al. (2015) Dynamic contrast-enhanced MRI of the prostate with high spatiotemporal resolution using compressed sensing, parallel imaging, and continuous golden-angle radial sampling: preliminary experience. J Magn Reson Imaging 41(5):1365–1373. doi:10.1002/jmri.24661
103. Fennessy FM, McKay RR, Beard CJ, Taplin ME, Tempany CM (2014) Dynamic contrast-enhanced magnetic resonance imaging in prostate cancer clinical trials: potential roles and possible pitfalls. Transl Oncol 7(1):120–129
104. Rosenkrantz AB, Chandarana H, Hindman N, et al. (2013) Computed diffusion-weighted imaging of the prostate at 3 T: impact on image quality and tumour detection. Eur Radiol 23(11):3170–3177. doi:10.1007/s00330-013-2917-8
105. Verma S, Turkbey B, Muradyan N, et al. (2012) Overview of dynamic contrast-enhanced MRI in prostate cancer diagnosis and management. Am J Roentgenol 198(6):1277–1288. doi:10.2214/AJR.12.8510
106. Alonzi R, Padhani AR, Allen C (2007) Dynamic contrast enhanced MRI in prostate cancer. Eur J Radiol 63(3):335–350. doi:10.1016/j.ejrad.2007.06.028
107. Girouin N, Mege-Lechevallier F, Tonina Senes A, et al. (2007) Prostate dynamic contrast-enhanced MRI with simple visual diagnostic criteria: is it reasonable? Eur Radiol 17(6):1498–1509. doi:10.1007/s00330-006-0478-9
108. Hansford BG, Peng Y, Jiang Y, et al. (2015) Dynamic Contrast-enhanced MR Imaging Curve-type Analysis: Is It Helpful in the Differentiation of Prostate Cancer from Healthy Peripheral Zone? Radiology 275(2):448–457. doi:10.1148/radiol.14140847
109. Ogura K, Maekawa S, Okubo K, et al. (2001) Dynamic endorectal magnetic resonance imaging for local staging and detection of neurovascular bundle involvement of prostate cancer: correlation with histopathologic results. Urology 57(4):721–726. doi:10.1016/S0090-4295(00)01072-4
110. Pallares J, Rojo F, Iriarte J, et al. (2006) Study of microvessel density and the expression of the angiogenic factors VEGF, bFGF and the receptors Flt-1 and FLK-1 in benign, premalignant and malignant prostate tissues. Histol Histopathol 21(8):857–865
111. Weidner N, Carroll PR, Flax J, Blumenfeld W, Folkman J (1993) Tumor angiogenesis correlates with metastasis in invasive prostate carcinoma. Am J Pathol 143(2):401–409
112. Isebaert S, De Keyzer F, Haustermans K, et al. (2012) Evaluation of semi-quantitative dynamic contrast-enhanced MRI parameters for prostate cancer in correlation to whole-mount histopathology. Eur J Radiol 81(3):e217–222. doi:10.1016/j.ejrad.2011.01.107
113. Oto A, Yang C, Kayhan A, et al. (2011) Diffusion-weighted and dynamic contrast-enhanced MRI of prostate cancer: correlation of quantitative MR parameters with Gleason score and tumor angiogenesis. Am J Roentgenol 197(6):1382–1390. doi:10.2214/AJR.11.6861
114. Peng Y, Jiang Y, Yang C, et al. (2013) Quantitative analysis of multiparametric prostate MR images: differentiation between prostate cancer and normal tissue and correlation with Gleason score–a computer-aided diagnosis development study. Radiology 267(3):787–796. doi:10.1148/radiol.13121454
115. Hegde JV, Mulkern RV, Panych LP, et al. (2013) Multiparametric MRI of prostate cancer: an update on state-of-the-art techniques and their performance in detecting and localizing prostate cancer. J Magn Reson Imaging 37(5):1035–1054. doi:10.1002/jmri.23860
116. Sourbron SP, Buckley DL (2011) On the scope and interpretation of the Tofts models for DCE-MRI. Magn Reson Med 66(3):735–745. doi:10.1002/mrm.22861
117. Sourbron SP, Buckley DL (2013) Classic models for dynamic contrast-enhanced MRI. NMR Biomed 26(8):1004–1027. doi:10.1002/nbm.2940
118. Tofts PS, Brix G, Buckley DL, et al. (1999) Estimating kinetic parameters from dynamic contrast-enhanced T(1)-weighted MRI of a diffusable tracer: standardized quantities and symbols. J Magn Reson Imaging 10(3):223–232
119. Fennessy FM, Fedorov A, Gupta SN, et al. (2012) Practical considerations in T1 mapping of prostate for dynamic contrast enhancement pharmacokinetic analyses. Magn Reson Imaging 30(9):1224–1233. doi:10.1016/j.mri.2012.06.011

120. Fedorov A, Fluckiger J, Ayers GD, et al. (2014) A comparison of two methods for estimating DCE-MRI parameters via individual and cohort based AIFs in prostate cancer: a step towards practical implementation. Magn Reson Imaging 32(4):321–329. doi:10.1016/j.mri.2014.01.004
121. Port RE, Knopp MV, Brix G (2001) Dynamic contrast-enhanced MRI using Gd-DTPA: interindividual variability of the arterial input function and consequences for the assessment of kinetics in tumors. Magn Reson Med 45(6):1030–1038
122. Sanz-Requena R, Prats-Montalban JM, Marti-Bonmati L, et al. (2015) Automatic individual arterial input functions calculated from PCA outperform manual and population-averaged approaches for the pharmacokinetic modeling of DCE-MR images. J Magn Reson Imaging 42(2):477–487. doi:10.1002/jmri.24805
123. Ortuno JE, Ledesma-Carbayo MJ, Simoes RV, et al. (2013) DCE@urLAB: a dynamic contrast-enhanced MRI pharmacokinetic analysis tool for preclinical data. BMC Bioinform 14:316. doi:10.1186/1471-2105-14-316
124. Schmid VJ, Whitcher B, Padhani AR, Taylor NJ, Yang GZ (2006) Bayesian methods for pharmacokinetic models in dynamic contrast-enhanced magnetic resonance imaging. IEEE Trans Med Imaging 25(12):1627–1636
125. Schmid VJ, Whitcher B, Padhani AR, Taylor NJ, Yang GZ (2009) A Bayesian hierarchical model for the analysis of a longitudinal dynamic contrast-enhanced MRI oncology study. Magn Reson Med 61(1):163–174. doi:10.1002/mrm.21807
126. Smith DS, Li X, Arlinghaus LR, Yankeelov TE, Welch EB (2015) DCEMRI.jl: a fast, validated, open source toolkit for dynamic contrast enhanced MRI analysis. PeerJ 3:e909. doi:10.7717/peerj.909
127. Zollner FG, Weisser G, Reich M, et al. (2013) UMMPerfusion: an open source software tool towards quantitative MRI perfusion analysis in clinical routine. J Digital Imaging 26(2):344–352. doi:10.1007/s10278-012-9510-6
128. Kurhanewicz J, Vigneron DB, Hricak H, et al. (1996) Prostate cancer: metabolic response to cryosurgery as detected with 3D H-1 MR spectroscopic imaging. Radiology 200(2):489–496
129. Shukla-Dave A, Hricak H, Moskowitz C, et al. (2007) Detection of prostate cancer with MR spectroscopic imaging: an expanded paradigm incorporating polyamines. Radiology 245(2):499–506. doi:10.1148/radiol.2452062201
130. Costello LC, Franklin RB (1991) Concepts of citrate production and secretion by prostate. 1. Metabolic relationships. Prostate 18(1):25–46
131. Costello LC, Franklin RB (1998) Novel role of zinc in the regulation of prostate citrate metabolism and its implications in prostate cancer. Prostate 35(4):285–296
132. Kaji Y, Kurhanewicz J, Hricak H, et al. (1998) Localizing prostate cancer in the presence of postbiopsy changes on MR images: role of proton MR spectroscopic imaging. Radiology 206(3):785–790
133. Kurhanewicz J, Vigneron DB (2008) Advances in MR spectroscopy of the prostate. Magn Reson Imaging Clin N Am 16(4): 697–710, ix–x. doi:10.1016/j.mric.2008.07.005
134. Kurhanewicz J, Vigneron DB, Hricak H, et al. (1996) Three-dimensional H-1 MR spectroscopic imaging of the in situ human prostate with high (0.24–0.7-cm3) spatial resolution. Radiology 198(3): 795–805
135. Ackerstaff E, Pflug BR, Nelson JB, Bhujwalla ZM (2001) Detection of increased choline compounds with proton nuclear magnetic resonance spectroscopy subsequent to malignant transformation of human prostatic epithelial cells. Cancer Res 61(9): 3599–3603
136. Hricak H (2005) MR imaging and MR spectroscopic imaging in the pre-treatment evaluation of prostate cancer. Br J Radiol 78 Spec No 2:S103–111. doi:10.1259/bjr/11253478
137. Podo F (1999) Tumour phospholipid metabolism. NMR Biomed 12(7):413–439
138. Kurhanewicz J, Swanson MG, Nelson SJ, Vigneron DB (2002) Combined magnetic resonance imaging and spectroscopic imaging approach to molecular imaging of prostate cancer. J Magn Reson Imaging 16(4):451–463
139. Ganie FA, Wani MS, Shaheen F, et al. (2013) Endorectal coil MRI and MR-spectroscopic imaging in patients with elevated serum prostate specific antigen with negative trus transrectal ultrasound guided biopsy. Urology annals 5(3):172–178. doi:10.4103/0974-7796.115741
140. Kobus T, Wright AJ, Scheenen TW, Heerschap A (2014) Mapping of prostate cancer by 1H MRSI. NMR Biomed 27(1):39–52. doi:10.1002/nbm.2973
141. Cunningham CH, Vigneron DB, Chen AP, et al. (2005) Design of flyback echo-planar readout gradients for magnetic resonance spectroscopic imaging. Magn Reson Med 54(5):1286–1289. doi:10.1002/mrm.20663
142. Lagemaat MW, Breukels V, Vos EK, et al. (2015) H MR spectroscopic imaging of the prostate at 7T using spectral-spatial pulses. Magn Reson Med . doi:10.1002/mrm.25569
143. Tran TK, Vigneron DB, Sailasuta N, et al. (2000) Very selective suppression pulses for clinical MRSI studies of brain and prostate cancer. Magn Reson Med 43(1):23–33
144. Males RG, Vigneron DB, Star-Lack J, et al. (2000) Clinical application of BASING and spectral/spatial water and lipid suppression pulses for prostate cancer staging and localization by in vivo 3D 1H magnetic resonance spectroscopic imaging. Magn Reson Med 43(1):17–22
145. Star-Lack J, Nelson SJ, Kurhanewicz J, Huang LR, Vigneron DB (1997) Improved water and lipid suppression for 3D PRESS CSI using RF band selective inversion with gradient dephasing (BASING). Magn Reson Med 38(2):311–321
146. Schricker AA, Pauly JM, Kurhanewicz J, Swanson MG, Vigneron DB (2001) Dualband spectral-spatial RF pulses for prostate MR spectroscopic imaging. Magn Reson Med 46(6):1079–1087
147. Cunningham CH, Vigneron DB, Chen AP, et al. (2004) Design of symmetric-sweep spectral-spatial RF pulses for spectral editing. Magn Reson Med 52(1):147–153. doi:10.1002/mrm.20116
148. Crane JC, Olson MP, Nelson SJ (2013) SIVIC: Open-Source, Standards-Based Software for DICOM MR Spectroscopy Workflows. Int J Biomed Imaging 2013:169526. doi:10.1155/2013/169526
149. Maudsley AA, Darkazanli A, Alger JR, et al. (2006) Comprehensive processing, display and analysis for in vivo MR spectroscopic imaging. NMR Biomed 19(4):492–503. doi:10.1002/nbm.1025
150. Wilson M, Reynolds G, Kauppinen RA, Arvanitis TN, Peet AC (2011) A constrained least-squares approach to the automated quantitation of in vivo (1)H magnetic resonance spectroscopy data. Magn Reson Med 65(1):1–12. doi:10.1002/mrm.22579
151. Nelson SJ, Brown TR (1989) A study of the accuracy of quantification which can be obtained from 1-D NMR spectra using the PIQABLE algorithm. J Magn Reson 84(1):95–109
152. Jung JA, Coakley FV, Vigneron DB, et al. (2004) Prostate depiction at endorectal MR spectroscopic imaging: investigation of a standardized evaluation system. Radiology 233(3):701–708
153. Futterer JJ, Scheenen TW, Heijmink SW, et al. (2007) Standardized threshold approach using three-dimensional proton magnetic resonance spectroscopic imaging in prostate cancer localization of the entire prostate. Invest Radiol 42(2):116–122. doi:10.1097/01.rli.0000251541.03822.bb
154. Kobus T, Hambrock T, Hulsbergen-van de Kaa CA, et al. (2011) In vivo assessment of prostate cancer aggressiveness using magnetic resonance spectroscopic imaging at 3 T with an endorectal coil. Eur Urol 60(5):1074–1080. doi:10.1016/j.eururo.2011.03.002
155. Selnaes KM, Gribbestad IS, Bertilsson H, et al. (2013) Spatially matched in vivo and ex vivo MR metabolic profiles of prostate cancer: investigation of a correlation with Gleason score. NMR Biomed 26(5):600–606. doi:10.1002/nbm.2901
156. Verma S, Rajesh A, Futterer JJ, et al. (2010) Prostate MRI and 3D MR spectroscopy: how we do it. Am J Roentgenol 194(6): 1414–1426. doi:10.2214/AJR.10.4312/AJR.10.4312
157. Sciarra A, Panebianco V, Ciccariello M, et al. (2010) Magnetic resonance spectroscopic imaging (1H-MRSI) and dynamic contrast-enhanced magnetic resonance (DCE-MRI): pattern changes from inflammation to prostate cancer. Cancer Invest 28(4):424–432. doi:10.3109/07357900903287048
158. Shukla-Dave A, Hricak H, Eberhardt SC, et al. (2004) Chronic prostatitis: MR imaging and 1H MR spectroscopic imaging findings–initial observations. Radiology 231(3):717–724. doi:10.1148/radiol.2313031391

159. Dosda R, Marti-Bonmati L, Ronchera-Oms CL, Molla E, Arana E (2003) Effect of subcutaneous butylscopolamine administration in the reduction of peristaltic artifacts in 1.5-T MR fast abdominal examinations. Eur Radiol 13(2):294–298. doi:10.1007/s00330-002-1500-5
160. Roethke MC, Kuru TH, Radbruch A, Hadaschik B, Schlemmer HP (2013) Prostate magnetic resonance imaging at 3 Tesla: is administration of hyoscine-N-butyl-bromide mandatory? World J Radiol 5(7):259–263. doi:10.4329/wjr.v5.i7.259
161. Wagner M, Rief M, Busch J, et al. (2010) Effect of butylscopolamine on image quality in MRI of the prostate. Clin Radiol 65(6):460–464. doi:10.1016/j.crad.2010.02.007
162. Lim C, Quon J, McInnes M, et al. (2014) Does a cleansing enema improve image quality of 3T surface coil multiparametric prostate MRI? J Magn Reson Imaging . doi:10.1002/jmri.24833
163. Medved M, Sammet S, Yousuf A, Oto A (2014) MR imaging of the prostate and adjacent anatomic structures before, during, and after ejaculation: qualitative and quantitative evaluation. Radiology 271(2):452–460. doi:10.1148/radiol.14131374
164. Dickinson L, Ahmed HU, Allen C, et al. (2011) Magnetic resonance imaging for the detection, localisation, and characterisation of prostate cancer: recommendations from a European consensus meeting. Eur Urol 59(4):477–494. doi:10.1016/j.eururo.2010.12.009
165. Kirkham AP, Haslam P, Keanie JY, et al. (2013) Prostate MRI: who, when, and how? Report from a UK consensus meeting. Clin Radiol 68(10):1016–1023. doi:10.1016/j.crad.2013.03.030
166. Kitajima K, Kaji Y, Fukabori Y, et al. (2010) Prostate cancer detection with 3 T MRI: comparison of diffusion-weighted imaging and dynamic contrast-enhanced MRI in combination with T2-weighted imaging. J Magn Reson Imaging 31(3):625–631. doi:10.1002/jmri.22075